RSC Advances

PAPER

View Article Online
View Journal | View Issue

Cite this: *RSC Adv.*, 2025, **15**, 41351

Enhanced elimination of Cr(VI) by sulphidated nanoscale zero valent iron biochar composites: performance and mechanism

Meijuan Kuang,†[b] Qi Qin,†[a] Yun Li,[a] Jiayi Lian,[a] Changjiang Yu,*[a] Hui Yu,[a] Tiantian Peng,[a] Zhenya Jia,[c] Xiaomao Song*[b] and Liantong Wang[a]

Received 20th July 2025
Accepted 9th October 2025

DOI: 10.1039/d5ra05234c

rsc.li/rsc-advances

Nanoscale zero-valent iron–biochar (BC@Fe) composites were synthesised *via* a one-step carbothermal method, followed by sulphidation to obtain sulphided BC@Fe (S-nZVI/BC-C-*X*) composites. Sulphidated nanoscale zero-valent iron–biochar (S-nZVI/BC-B-*X*) was also prepared using a one-step sodium borohydride reduction method. Batch experiments were conducted to investigate the effects of adsorption time, initial Cr(VI) concentration, pH and background ions on the Cr(VI) removal performance of S-nZVI/BC-C-*X* and S-nZVI/BC-B-*X*. A comparative analysis of their adsorption characteristics and removal efficiencies was conducted. The adsorption mechanisms were further elucidated through kinetic and isotherm model fitting, masking experiments and characterisation of the composites before and after Cr(VI) adsorption. The findings revealed that Cr(VI) removal by S-nZVI/BC-C-5 primarily occurred *via* (i) reduction of Cr(VI) to Cr(III) by FeS, FeS_2 and Fe^0, (ii) reduction of Cr(VI) to Cr(III) by Fe^{2+}, (iii) reduction of Cr(VI) to Cr(III) by HS^- released from FeS corrosion and (iv) adsorption of Cr(VI) by S-nZVI/BC-C-5.

1. Introduction

China is the world's largest producer of chromium chemicals, and the discharge of chromium-containing wastewater from processes such as electroplating and tanning and from the chemical manufacturing industry has led to substantial chromium pollution.[1] In the environment, chromium exists primarily in two forms: Cr(III) and Cr(VI). Cr(VI) is 100 times more toxic than Cr(III). According to China's GB 5749-2022 standard for drinking water quality, the maximum permissible level of Cr(VI) in drinking water is 0.05 mg L^{-1}. Cr(VI) is known for its carcinogenic, teratogenic and mutagenic effects, posing serious threats to human health and ecosystems.[2] Consequently, addressing Cr(VI) pollution has become a pressing environmental issue.

The primary approaches for Cr(VI) pollution remediation are chemical reduction, adsorption and microbial remediation.[3] Among these approaches, chemical reduction is currently the most mature, well-established and widely applied technique in engineering applications owing to its cost-effectiveness and high efficiency.[4] Commonly used reducing agents include iron-based reductants (*e.g.* Fe^0), sulphur-based reductants (*e.g.* CaS), organic reductants and biochar.[4] Nanoscale zero-valent iron (nZVI) has garnered considerable research attention for environmental remediation owing to its high adsorption capacity, strong reducibility and rapid reaction rates.[5,6] However, nZVI presents certain limitations in addressing environmental remediation, such as pH dependence, poor electron selectivity, susceptibility to agglomeration, oxidation and passivation.[7] In addition, nZVI easily reacts with water, oxygen or other ions during the adsorption process, leading to a reduction in its removal capacity.[8]

To improve the performance of nZVI for pollutant removal, its surface or structure is typically modified using physical or chemical methods. Currently, the primary modification techniques for nZVI are coating,[9] loading,[10,11] bimetallic structure formation[12] and vulcanisation.[13] Among these techniques, sulphide modification has proved particularly effective in enhancing the pollutant removal efficiency and long-term reactivity of nZVI.[14] Sulphidated nZVI (S-nZVI) offers considerable advantages for the remediation of water and soil pollution. FeS can simultaneously release two reducing ions—Fe(II) and S^{2-}—which function as electron donors during Cr(VI) reduction.[15]

Carbon materials, such as activated carbon and biochar, serve as excellent carriers and adsorbents. When composited with S-nZVI particles, carbon materials (i) prevent the

[a]*Key Laboratory of Water Pollution Treatment & Resource Reuse of Hainan Province, Key Laboratory of Natural Polymer Function Material of Haikou City, College of Chemistry and Chemical Engineering, Hainan Normal University, No. 99 Longkunnan Road, Haikou 571158, China. E-mail: ycjhnsfdx@163.com*

[b]*Haikou Engineering Technology Research Center of Solid Waste Treatment & Disposal and Soil Remediation, Hainan Pujin Environmental Technology Co., Ltd, Haikou 570105, China. E-mail: 18976757399@163.com*

[c]*Hainan Huantai Environmental Resources Co., Ltd, Haikou 571158, China*

† These authors contributed equally to this work.

aggregation and deactivation of these particles by dispersing and stabilising them and (ii) efficiently adsorb and concentrate Cr(VI) on their surfaces,[10] thereby providing them with a highly reactive interface. Furthermore, the conductive nature of carbon facilitates electron transfer and thereby enhances the Cr(VI) reduction process.[16,17] The resulting Cr(III) is subsequently adsorbed or precipitated onto the composite material.

Yang *et al.* demonstrated that an ultra-high-dispersion S-nZVI carbon nanotube–polyacrylonitrile honeycomb membrane efficiently removed Cr(VI) and exhibited strong resistance to interference from Cl^-, NO_3^-, HCO_3^- and SO_4^{2-}.[13] Tian *et al.* synthesised a novel S-nZVI supported on polyethyleneimine-modified corn straw biochar, which outperformed conventional nZVI in terms of stability and reusability, making it more promising for environmental applications.[18]

S-nZVI is primarily prepared *via* liquid-phase reduction through one-step or two-step sulphidation.[14,19] However, the selection of alternative reductants to the commonly used $NaBH_4$, which is expensive and forms numerous secondary pollutants during reduction,[20] is essential for the effective remediation of Cr(VI) pollution. Moreover, S-nZVI supported on porous materials through $NaBH_4$ reduction has a limited loading capacity, which constrains its pollutant removal efficiency. An emerging S-nZVI synthesis approach involves the use of sulphide-reducing bacteria; however, the conditions and processes involved in this approach are considerably complex.[21,22] In Cr(VI) pollution remediation engineering, the cost-effectiveness of materials is a critical factor. Therefore, developing economical and eco-friendly S-nZVI is imperative for current environmental remediation efforts.

In this study, sodium alginate (SA) was crosslinked with Fe^{3+} to obtain an SA–Fe^{3+} gel with a three-dimensional network structure. nZVI biochar (Fe@BC) composites were prepared *via* high-temperature pyrolysis of the SA–Fe^{3+} gel. Furthermore, S-nZVI biochar (S-nZVI/BC-C-*X*) was prepared by sulphidising Fe@BC. The Cr(VI) removal performance of S-nZVI/BC-C-*X* was then systematically compared with that of S-nZVI biochar synthesised *via* $NaBH_4$ reduction (S-nZVI/BC-B-*X*).

The main objectives of our study were as follows: (1) development of an economical and green method for preparing S-nZVI, (2) comparison of Cr(VI) removal performance between S-nZVI/BC-C-*X* and S-nZVI/BC-B-*X* and (3) investigation of the Cr(VI) remediation mechanism of S-nZVI/BC-C-*X* and S-nZVI/BC-B-*X*. Thus, this study offers a method for preparing S-nZVI, which has promising applications for the remediation of Cr(VI)-contaminated water and soil contamination.

2. Materials and methods

2.1 Materials

SA, $FeCl_3 \cdot 6H_2O$, tartaric acid, ascorbic acid, and oxalic acid (all AR) were obtained from Aladdin. NaOH (AR) was obtained from Shanghai Yi En Chemical Technology Co., Ltd. NaCl, Na_2CO_3, Na_2SO_4 and $NaNO_3$ (all AR) were procured from Shanghai Baishun Biotechnology Co., Ltd. $Na_2S \cdot 9H_2O$, $K_2Cr_2O_7$, H_3PO_4, H_2SO_4, HNO_3 and $NaBH_4$ were provided by Guangdong Xilong Chemical Co., Ltd. Furthermore, 1,10-phenanthroline (AR) was provided by Shanghai Aladdin Biochemical Technology Co., Ltd., and 1,5-diphenylcarbazide (AR) was obtained from Shanghai MacLean Biochemical Technology Co. Ltd. *o*-Phthalic anhydride (AR) were procured from Guangdong Yuefeng Chemical Reagent Co., Ltd. Finally, standard solutions of Fe and Cr^{6+} were obtained from China National Academy of Metrology Sciences, and the pH buffer reagent were obtained from Aipure.

2.2 Characterisation

Transmission electron microscopy (TEM; JEM-2100Plus, JEOL, Japan) was performed at an accelerating voltage of 200 kV. The S-nZVI/BC-C-5 and S-nZVI/BC-B-5 for TEM measurement was prepared by dispersing a small quantity of the powder sample in ethanol *via* ultrasonication for 10 min. A droplet of the resulting suspension was subsequently transferred onto an ultrathin carbon-supported film and dried at ambient conditions prior to the analysis. X-ray diffraction (XRD; UItima IV, Rigaku, Japan) was conducted under the following test conditions: light source = Cu Kα, wavelength = 0.15418 nm, operating voltage = 40 kV, operating current = 10 mA and scanning range 2θ = 10–80°. An instrument measuring the adsorption specific surface area and pore-size distribution (Tristar II 3020, Micromeritics, USA) was used in adsorption tests. X-ray photoelectron spectroscopy (XPS; ESCALAB 250Xi) was performed under the following test conditions: light source = AI Kα ($h\nu$ = 1486.6 eV) and power = 150 W; moreover, a 500 μm-beam-spot energy analyser with a fixed transmission energy of 30 eV (Thermo Corporation, USA) was used for performing XPS. The S-nZVI/BC-C-5 and S-nZVI/BC-B-5 for XPS analysis were prepared using the pressed pellet method. First, a piece of conductive tape with an area of 1 × 1 cm^2 was attached to a clean aluminium foil substrate. The dry powder was then evenly distributed onto the adhesive surface. The sample was encapsulated with a second piece of aluminium foil and pressed into a pellet under pressure. Subsequently, the top foil was carefully removed and the excess foil around the pellet was trimmed away. The obtained pellet was mounted on a sample stub for XPS measurement. Further, a tube furnace (OTF1200X, Hefei Kejing Material Technology Co., Ltd), atomic absorption spectrophotometer (AA-7000, Shimadzu, Japan) and ultraviolet-visible (UV-vis) spectrophotometer (UV-2700, Shimadzu, Japan) were used.

2.3 Preparation of S-nZVI/BC-C-*X*

SA (30 g) was dissolved in distilled water (1 L) by stirring in a beaker. Then, a $FeCl_3$ solution (0.3 mol L^{-1}) was prepared, and SA was dropped into it for cross-linking by allowing the mixture to stand for 24 h. The resulting SA–Fe^{3+} gel was filtered and washed with distilled water 6–8 times to remove Fe^{3+} from the surface. The gel was then dried in a vacuum drying oven at 60 °C and baked at 100 °C for 3 h. The dried gel was then placed in a crucible and kept in a tube furnace. After vacuuming for 15 min, high-purity nitrogen was passed through the chamber at a flow rate of 200 mL min^{-1} for 20 min. Subsequently, temperature was first increased to 200 °C and then to 900 °C at

heating rates of 5 °C min^{-1} and 10 °C min^{-1}, respectively, while maintaining a nitrogen flow rate of 100 mL min^{-1}. The reaction mixture was then allowed to cool to room temperature at a rate of 10 °C min^{-1}, followed by 3 h of pyrolysis at 900 °C. The obtained BC@Fe composite was bagged and stored under vacuum conditions.

$Na_2S·9H_2O$ (2.5739 g) was dissolved in 50 mL of deionised water in a conical flask. Then, 1 g of BC@Fe was added to the mixture and shaken at 25 °C and 120 rpm for 2 h. After filtration and separation, the product was vacuum-dried at 50 °C to obtain S-nZVI/BC-C-5, which was stored in a vacuum desiccator. Under the same conditions, the amounts of $Na_2S·9H_2O$ added were adjusted to 7.2436 and 0.5148 g to prepare sulphided BC@Fe (S-nZVI/BC-C-*X*), labelled as S-nZVI/BC-C-10 and S-nZVI/BC-C-1, respectively.

2.4 Preparation of S-nZVI/BC-B-*X*

Coconut shells were dried, crushed, and sieved through a 200-mesh sieve and dried again at 100 °C for 2 h. The powder was placed in a tube furnace, evacuated and purged with nitrogen. The temperature was raised to 200 °C at a heating rate of 5 °C min^{-1}, then further increased to 700 °C at 10 °C min^{-1} and held at 700 °C for 3 h for pyrolysis. The sample was then cooled to room temperature at 10 °C min^{-1}. The resulting coconut shell biochar was washed with 250 mL of 5 mol per L HNO_3 in a 500 mL conical flask and shaken for 3 h at 120 rpm and 25 °C for 3 h. After filtration and rinsing, the pH was adjusted to 7 and the material was dried at 80 °C to obtain coconut shell-activated carbon. To synthesise S-nZVI/BC-B-5, 0.9 g of coconut shell-activated carbon was added to a three-necked flask, followed by 125 mL of a 0.045 mol per L $FeCl_3$ solution under nitrogen protection. After stirring for 30 min, a mixed solution of 0.00225 mol per L Na_2S and 0.25 mol per L $NaBH_4$ (125 mL, prepared in an anaerobic bottle) was slowly added using a peristaltic pump. The reaction mixture was stirred for 30 min, and the product was collected *via* vacuum filtration and dried in a freeze dryer for 24 h. The composite was stored in a vacuum-sealed bag. S-nZVI/BC-B-1 and S-nZVI/BC-B-10 were similarly prepared using $Na_2S·9H_2O$ concentrations of 0.0009 and 0.0045 mol L^{-1}, respectively. nZVI biochar (nZVI/BC) was synthesised under identical conditions but without Na_2S addition.

2.5 Comparison of S-nZVI/BC-C-*X* and S-nZVI/BC-B-*X* for Cr(VI) adsorption

A Cr(VI) solution with pH 2 and a mass concentration of 50 mg L^{-1} was prepared for tests. Further, 100 mL of the Cr(VI) solution was added to 15 mg of S-nZVI/BC-C-5 in a conical flask. The solution thus obtained was shaken at 25 °C and 120 rpm for 24 h, allowing adsorption. The concentration of Cr(VI) was determined using an UV-vis spectrophotometer.[23] The experimental conditions of Cr(VI) adsorption on BC@Fe, S-nZVI/BC-C-*X*, nZVI/BC and S-nZVI/BC-B-*X* were the same as those for S-nZVI/BC-C-5. Each set of experiments was repeated thrice.

2.6 The effect of initial pH level on the adsorption of Cr(VI) by S-nZVI/BC-C-5 and S-nZVI/BC-B-5

A 50 mg per L Cr(VI) solution was prepared, and its pH was adjusted to 2, 3, 4, 5, 6 and 7 in separate aliquots. Then, Cr(VI) solution aliquots (100 mL each) with different pH levels were separately mixed with 15 mg of S-nZVI/BC-C-5 in a conical flask. The solution was shaken at 25 °C and 120 rpm for 24 h. The Cr(VI) concentration was determined after completion of adsorption.[24] Each experiment was repeated three times for each pH level. The experimental conditions for Cr(VI) adsorption on S-nZVI/BC-B-5 were the same as those used for S-nZVI/BC-C-5.

2.7 Kinetic Cr(VI) adsorption experiments for S-nZVI/BC-C-5 and S-nZVI/BC-B-5

A Cr(VI) solution with pH 2 and a mass concentration of 50 mg L^{-1} was prepared. Then, 500 mL of the Cr(VI) solution was added to a conical flask with 75 mg of S-nZVI/BC-C-5. The conical flask was shaken at 25 °C and 120 rpm. Subsequently, 1 mL of the Cr(VI) solution was sampled at predetermined time intervals, and the Cr(VI) concentration was determined after dilution.[23,25] The same experiment was repeated, with sampling times ranging from 1 to 48 h. The experiments were replicated thrice for each time point. The kinetic Cr(VI) adsorption experiment for S-nZVI/BC-B-5 was conducted under the same conditions as for S-nZVI/BC-C-5, except that the sampling time intervals ranged from 10 min to 24 h.

The Cr(VI) adsorption capacity at time t (q_t) was calculated as follows:

$$q_t = \frac{(C_0 - C_t)V}{m}, \quad (1)$$

where C_0 (mg L^{-1}) is the initial Cr(VI) ion concentration, C_t (mg L^{-1}) is the Cr(VI) ion concentration at time t, V is the volume (L) of Cr(VI) ion solution and m is the dry mass (g) of the adsorbent.

2.8 Isotherm Cr(VI) adsorption experiments for S-nZVI/BC-C-5 and S-nZVI/BC-B-5

Adsorption isotherm experiments were performed by adding 15 mg of S-nZVI/BC-C-5 to 100 mL of a Cr(VI) solution with varying initial concentrations (50, 100, 200 and 300 mg L^{-1}) at pH 2. The mixtures were shaken at 120 rpm and 25 °C for 24 h. The isotherm Cr(VI) adsorption experiments for S-nZVI/BC-B-5 were conducted under the same conditions as those for S-nZVI/BC-C-5.

The adsorption capacity at the adsorption equilibrium (q_e) was calculated as follows:

$$q_e = \frac{(C_0 - C_e)V}{m}, \quad (2)$$

where C_0 (mg L^{-1}) and C_e are the initial and equilibrium concentrations of Cr(VI) ions, respectively, V is the volume (L) of Cr(VI) solution and m is the dry mass (g) of adsorbent.

2.9 Cyclic Cr(VI) adsorption experiments for S-nZVI/BC-C-5 and S-nZVI/BC-B-5

In the cyclic adsorption experiments, 15 mg of S-nZVI/BC-C-5 was added to 100 mL of a 50 mg per L Cr(VI) solution at pH 2. The mixture was shaken at 25 °C and 120 rpm for 24 h to allow adsorption. After completion of adsorption, the solution was removed and 100 mL of a fresh Cr(VI) solution (50 mg L^{-1}; pH 2) was added to the same adsorbent to begin the next cycle. This process was repeated five times under identical conditions. The cyclic adsorption experiments for S-nZVI/BC-B-5 were conducted under the same conditions as those for S-nZVI/BC-C-5.

2.10 Masking experiments for Cr(VI) adsorption on S-nZVI/BC-C-5 and S-nZVI/BC-B-5

To investigate the role of Fe^{2+} in Cr(VI) adsorption, masking experiments were conducted using 1,10-phenanthroline as a chelating agent. A Cr(VI) solution (500 mL; 50 mg L^{-1}; pH 2) was prepared, and 1 g L^{-1} of 1,10-phenanthroline was added to this solution to mask Fe^{2+}. Then, 75 mg of S-nZVI/BC-C-5 was added to the solution. The mixture was shaken at 25 °C and 110 rpm. At predetermined time intervals (t = 1–24 h), 1 mL of the solution was sampled and analysed to determine the Cr(VI) concentration. The masking experiments for S-nZVI/BC-B-5 were performed under the same conditions as those for S-nZVI/BC-C-5, except with sampling intervals ranging from 30 min to 24 h.

2.11 Removal of simulated contaminants from water using S-nZVI/BC-C-5 and S-nZVI/BC-B-5

To evaluate the effect of background ions on Cr(VI) removal, Cr(VI) solutions (50 mg L^{-1}) were prepared either alone or in combination with various electrolytes, *i.e.* (i) 50 mmol per L NaCl, Na_2SO_4, $NaNO_3$ and KH_2PO_4 and (ii) 0.5 mmol per L tartaric acid, ascorbic acid, and oxalic acid. The pH of all solutions was adjusted to 2. Then, 200 mL of each solution was placed in a conical flask and a certain amount of S-nZVI/BC-C-5 was added. The mixture was shaken at 25 °C and 110 rpm for 24 h. After the reaction, a 1 mL aliquot of the solution was collected and analysed for Cr(VI) concentration using UV-vis spectroscopy. The same experimental procedure was applied to evaluate the effect of background ions on Cr(VI) adsorption by S-nZVI/BC-B-5.

2.12 Experiments on the remediation effect of S-nZVI/BC-C-5 on soil pollution by Cr(VI)

The soil sample was collected from Guilin Yang farm in Haikou. After drying, it was ground, crushed and sieved through a 100-mesh sieve. Then, 5.0 kg of soil was added to a certain amount of $K_2Cr_2O_7$ solution, dried naturally, milled, crushed and sieved through a 100-mesh sieve. The soil sample thus obtained was used as simulated Cr-contaminated soil (Cr(VI) concentration = 100 mg kg^{-1}).[26] Further, 10 g of the simulated soil sample was mixed with S-nZVI/BC-C-5 to obtain three separate mixtures (w/w = 1%, 2% and 3%). Deionised water was then added to increase the moisture content to 75%. The soil samples were stored away from light and weighed every 2 d. Water was added to maintain the soil moisture content. Soil was sampled and freeze-dried on the 14th and 28th day.[27] The Cr(VI) content was also determined *via* alkali extraction and atomic absorption.

3. Results and discussions

3.1 Material characterisation

Fig. 1a presents the SEM image of S-nZVI/BC-C-5. The surface of S-nZVI/BC-C-5 has a flocculent porous structure. This morphology is conducive to the entry of pollutants into the material. The high-resolution (HR) TEM (HRTEM) image of S-nZVI/BC-C-5 presented in Fig. 1b shows irregular metal particles. Fig. 1c shows the presence of lattice fringes with a crystallographic spacing of 0.26 nm; these correspond to the (112) crystallographic plane of FeS.[28] Fig. 1d shows lattice fringes with a crystallographic spacing of 0.34 nm that correspond to the (110) crystallographic plane of FeS_2.[29] The elemental mapping images of S-nZVI/BC-C-5 shown in Fig. 1e–h indicate dense distribution of C and uneven distribution of Fe and S. Fig. 1i confirms the successful loading of FeS and ZVI onto the biochar surface in S-nZVI/BC-B-5. As shown in Fig. 1j, the metal particles have a size of 100–300 nm. Fig. 1k and l further displays lattice fringes with a spacing of 0.25 nm, corresponding to the (201) plane of FeS.

Hysteresis loops are observed in the N_2 adsorption–desorption isotherms of S-nZVI/BC-C-5 and S-nZVI/BC-B-5 (Fig. 2a). According to the IUPAC classification, these N_2 adsorption–desorption isotherms are type IV curves and the observed hysteresis loops are H2-type curves.[30] The specific surface areas of S-nZVI/BC-C-5 and S-nZVI/BC-B-5 are determined to be 371 $m^2\ g^{-1}$ and 227.3 $m^2\ g^{-1}$, respectively. The pore-size distributions (Fig. 2b) reveal that S-nZVI/BC-C-5 and S-nZVI/BC-B-5 exhibit a microporous and mesoporous structure.[31] Moreover, the pore size is mainly distributed in 1–33 nm. The proportion of mesopores in the pore-size distribution is higher than that of micropores.

3.2 Comparison of the performance of S-nZVI/BC-C-*X* and S-nZVI/BC-B-*X* for Cr(VI) adsorption

S-nZVI/BC-C-*X*, S-nZVI/BC-B-*X*, nZVI/BC and BC@Fe are compared for their Cr(VI) adsorption performance, as shown in Fig. 3a. S-nZVI/BC-C-5 exhibits the highest adsorption capacity, whereas S-nZVI/BC-C-10 shows the lowest adsorption capacity. This behaviour may be attributed to the FeS content in the materials as a moderate level of FeS doping is known to enhance adsorption efficiency. Fig. 3b presents a comparison of Cr(VI) adsorption by S-nZVI/BC-B-*X* and nZVI/BC, revealing a similar trend to that observed in Fig. 3a. As the sulphur doping ratio increases, the Cr(VI) removal performance of S-nZVI/BC-B-*X* initially improves and then declines, with S-nZVI/BC-B-5 showing the optimal removal efficiency. These results indicate that both preparation methods benefit from an optimal sulphur doping level. However, S-nZVI/BC-C-5 exhibits superior Cr(VI) removal performance compared with S-nZVI/BC-B-5.

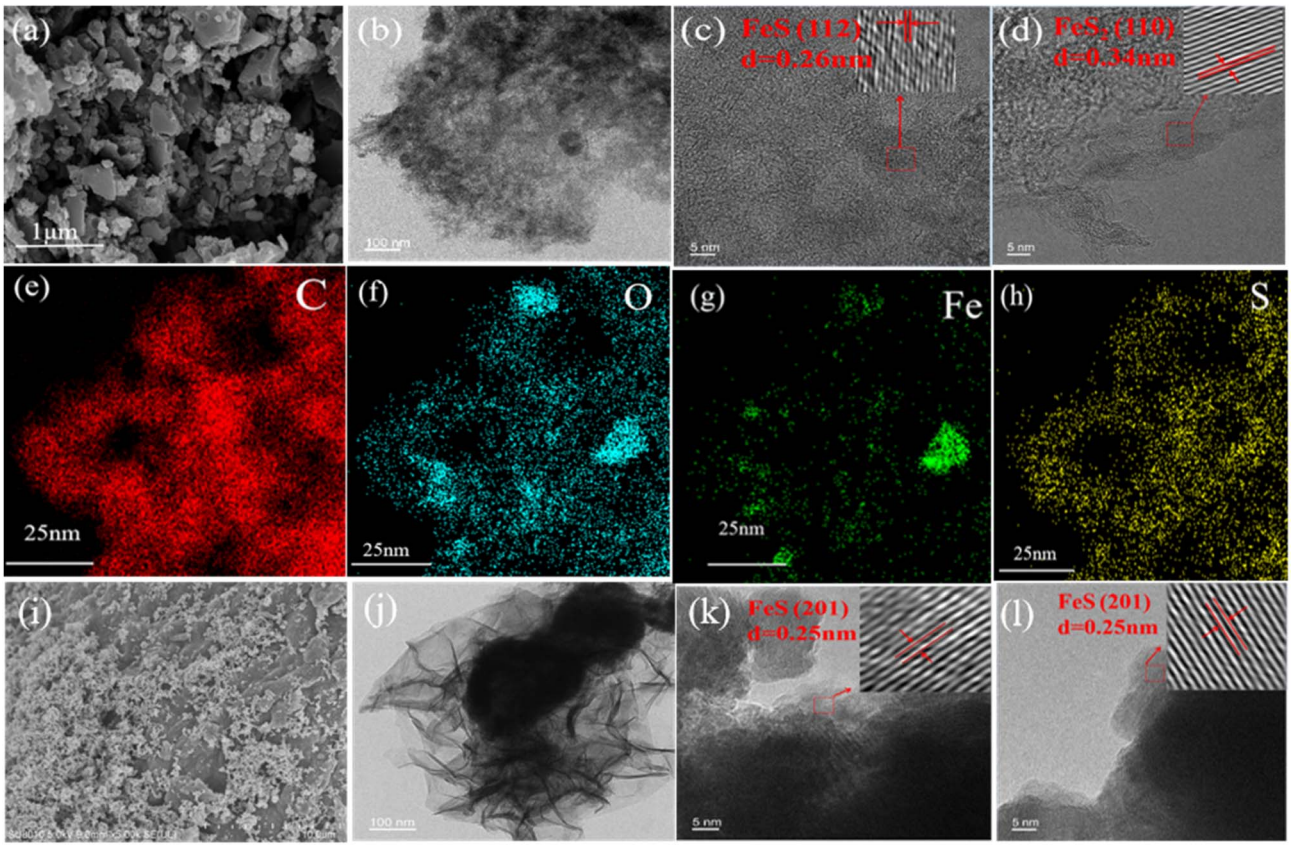

Fig. 1 (a) SEM, (b–d) HRTEM, and (e–h) HRTEM elemental mapping images of S-nZVI/BC-C-5; (i) SEM and (j–l) HRTEM images of S-nZVI/BC-B-5.

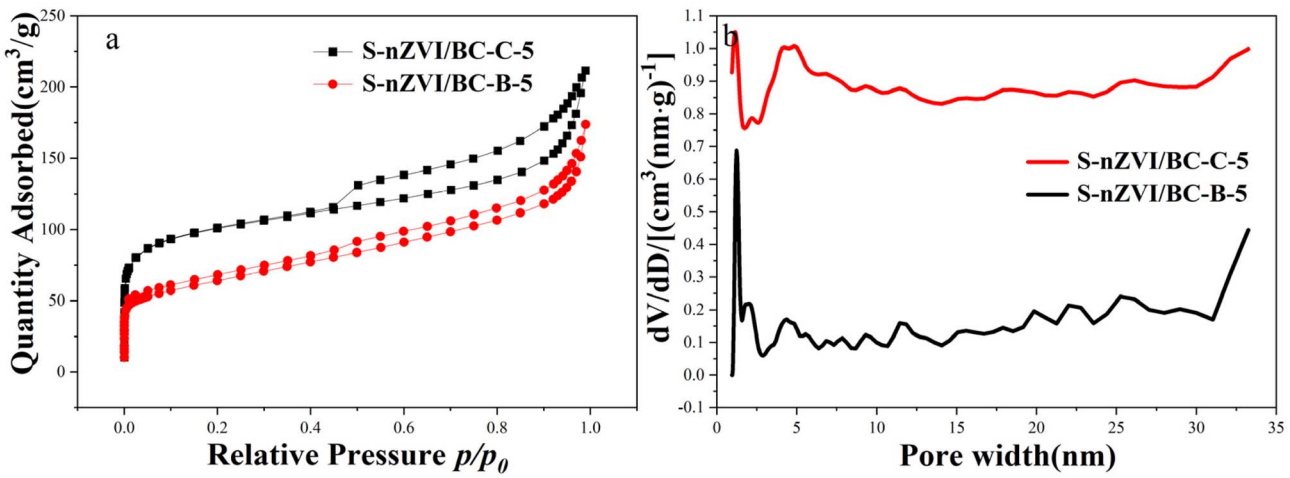

Fig. 2 BET (a) and pore-size analysis results (b) of S-nZVI/BC-C-5 and S-nZVI/BC-B-5.

3.3 Effect of pH on Cr(VI) adsorption by S-nZVI/BC-C-5 and S-nZVI/BC-B-5

Fig. 4 shows that the highest adsorption capacity of Cr(VI) was achieved by S-nZVI/BC-C-5 and S-nZVI/BC-B-5 at pH 2. This observation is mainly attributable to the strong acidic conditions, wherein a high concentration of H^+ promotes the corrosion of FeS and Fe into Fe^{2+}, which reduces Cr(VI) to Cr(III). With increasing pH, the Cr(VI) adsorption capacity of S-nZVI/BC-C-5 and S-nZVI/BC-B-5 decreases significantly.[32,33] After S-nZVI/BC-C-5 adsorb Cr(VI) at pH 2 and 3, the Fe ion concentrations in the solution are 4.7 and 0.28 mg L^{-1}, respectively. No Fe ions are detected in the solution after Cr(VI) adsorption by S-nZVI/BC-C-5 within the pH range of 4–7. When S-nZVI/BC-B-5 is used for Cr(VI) adsorption at pH 2, the Fe ion concentration in the solution is 0.83 mg L^{-1}, whereas no Fe ion is detected in the pH

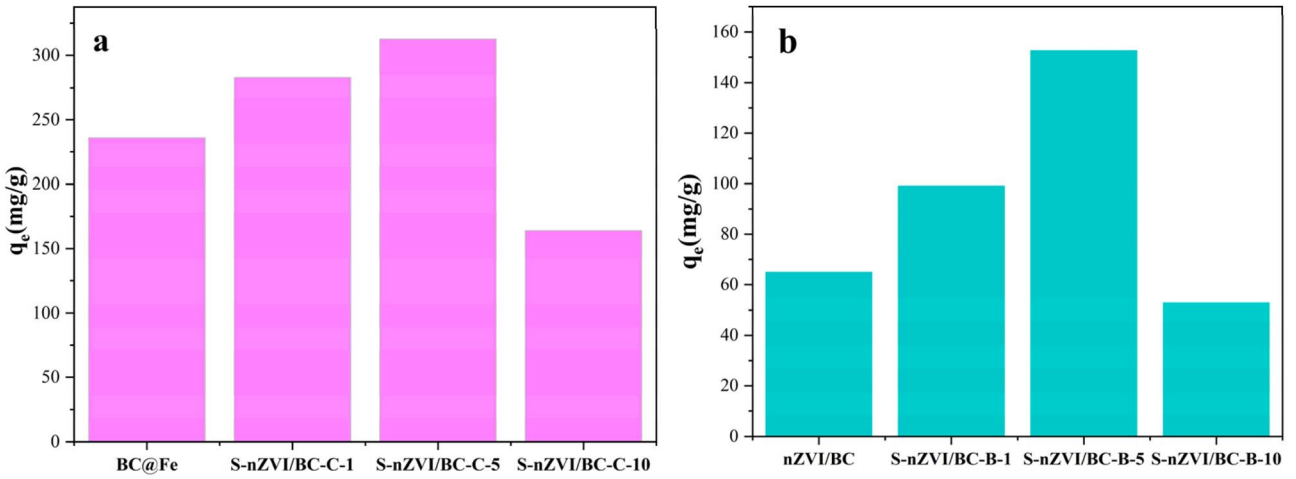

Fig. 3 Comparison of Cr(VI) adsorption performance among (a) S-nZVI/BC-C-*X* and BC@Fe, (b) S-nZVI/BC-B-*X* and nZVI/BC.

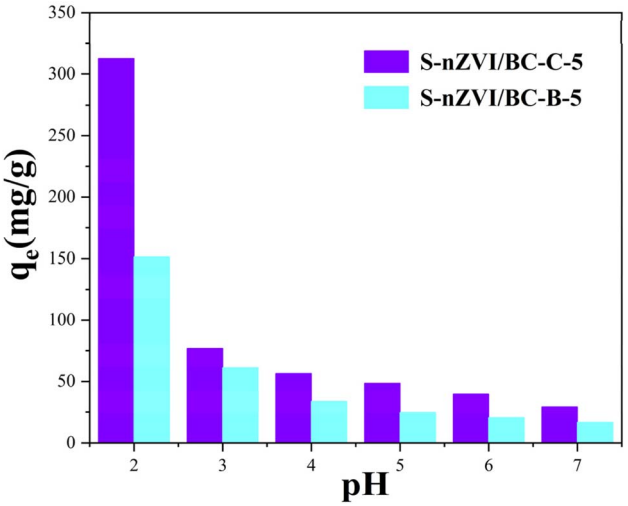

Fig. 4 Effect of pH on the adsorption of Cr(VI) by S-nZVI/BC-C-5 and S-nZVI/BC-B-5.

range of 3–7. At pH 2, S-nZVI/BC-C-5 and S-nZVI/BC-B-5 exhibit the highest metal dissolution, which is consistent with their superior Cr(VI) adsorption performance at the same pH. This indicates that the adsorption mechanism involves the corrosion-induced release of Fe^{2+} under acidic conditions and subsequent Cr(VI) reduction.[34]

3.4 Analysis of Cr(VI) adsorption kinetics for S-nZVI/BC-C-5 and S-nZVI/BC-B-5

The pseudo-first-order and pseudo-second-order kinetic models were used to fit the experimental data on Cr(VI) adsorption for S-nZVI/BC-C-5 and S-nZVI/BC-B-5 using eqn (3) and (4):[13,35–37]

$$q_t = q_e(1 - e^{-k_1 t}), \quad (3)$$

$$q_t = \frac{k_2 q_e^2 t}{1 + k_2 q_e t}, \quad (4)$$

where q_t is the adsorption capacity at time t (mg g^{-1}), q_e is the adsorption capacity at equilibrium (mg g^{-1}), k_1 is the first-order rate constant (min^{-1}), k_2 is the second-order rate constant (g mg^{-1} min^{-1}) and t is time (min).

Fig. 5 presents the fitting curves of Cr(VI) adsorption for S-nZVI/BC-C-5 and S-nZVI/BC-B-5 at pH 2. The rate of Cr(VI) adsorption for S-nZVI/BC-C-5 and S-nZVI/BC-B-5 is high before 6 h. At this stage, the redox reaction of FeS and Fe with Cr(VI) is the primary surface reaction.[38] Subsequently, the adsorption performance of S-nZVI/BC-B-5 for Cr(VI) decreases significantly, primarily because FeS and nZVI are mainly loaded on the surface of the biochar, leading to a rapid reaction during the adsorption process. The Cr(VI) adsorption on S-nZVI/BC-C-5 increases slowly after 6 h and reaches equilibrium at 24 h of adsorption, which can be primarily attributed to the spherical porous structure of S-nZVI/BC-C-5 facilitating the continuous reaction of FeS and nZVI with Cr(VI) inside the spheres.

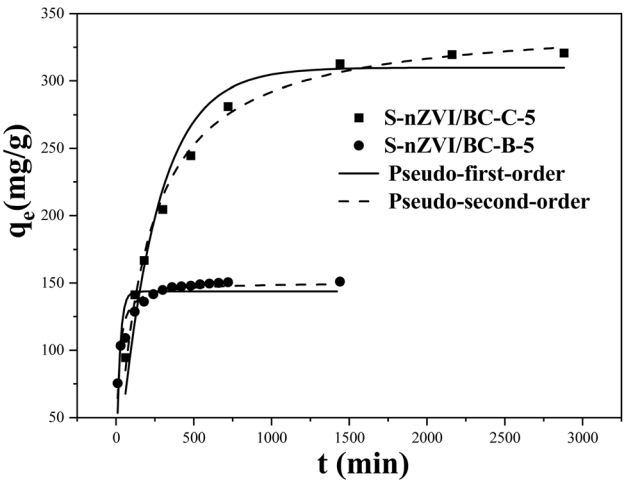

Fig. 5 Experiments on the kinetics of Cr(VI) adsorption by S-nZVI/BC-C-5 and S-nZVI/BC-B-5.

Table 1 Experimental fitted data of Cr(VI) adsorption kinetics

		Pseudo-first-order model			Pseudo-second-order model		
Materials	pH	$q_{e,cal}$ (mg g^{-1})	k_1	R^2	$q_{e,cal}$ (mg g^{-1})	k_2	R^2
S-nZVI/BC-C-5	2	309.8	0.00411	0.9540	345.6	0.0000157	0.9930
S-nZVI/BC-B-5	2	143.7	0.0467	0.7401	150.5	0.000497	0.9358

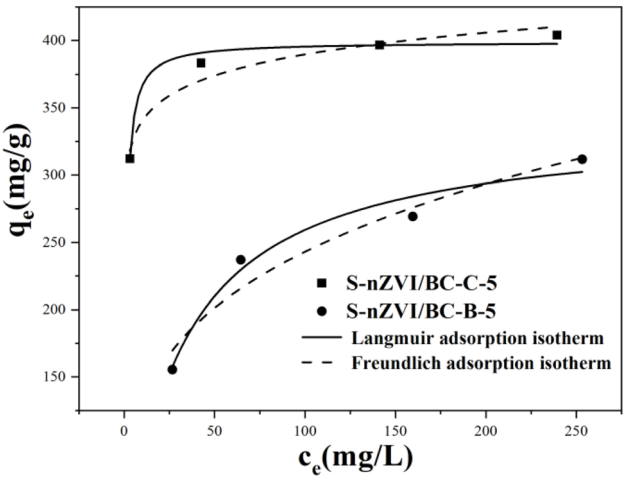

Fig. 6 Thermodynamic isotherms for Cr(VI) adsorption by S-nZVI/BC-C-5 and S-nZVI/BC-B-5 at pH 2.

The data fitting results of Cr(VI) adsorption for S-nZVI/BC-C-5 and S-nZVI/BC-B-5 are summarised in Table 1. At pH 2, the correlation coefficients (R^2) of the pseudo-second-order kinetic model of Cr(VI) adsorption for S-nZVI/BC-C-5 and S-nZVI/BC-B-5 were higher (0.9930 and 0.9358, respectively) than those of the pseudo-first-order kinetic model (0.9540 and 0.7401, respectively), indicating that Cr(VI) adsorption for S-nZVI/BC-C-5 and S-nZVI/BC-B-5 mainly involved chemisorption.[39,40]

3.5 Isothermal thermodynamic adsorption experiments

The data and fitted curves for Cr(VI) adsorption by S-nZVI/BC-C-5 and S-nZVI/BC-B-5 at pH 2 is shown in Fig. 6, and the fitting results are summarised in Table 2.

As shown in Table 2, the Langmuir adsorption model yields higher correlation coefficients (R^2 = 0.9721 and 0.9575 for S-nZVI/BC-C-5 and S-nZVI/BC-B-5, respectively) than the Freundlich model (R^2 = 0.9333 and 0.9194 for S-nZVI/BC-C-5 and S-nZVI/BC-B-5, respectively). In addition, the q_m values predicted by the Langmuir model align more closely with the experimental values.[41] These results suggest that the adsorption of Cr(VI) onto S-nZVI/BC-C-5 and S-nZVI/BC-B-5 primarily follows monolayer adsorption behaviour. According to the Langmuir model, the maximum adsorption quantities are 398.9 and 338.9 mg g^{-1} for S-nZVI/BC-C-5 and S-nZVI/BC-B-5, respectively. As summarized in Table 3, S-nZVI/BC-C-5 exhibits considerably higher Cr(VI) adsorption capacity than those of other reported adsorbents.

Table 2 Constants and correlation coefficients for the thermodynamic adsorption of Cr(VI) by S-nZVI/BC-C-5 and S-nZVI/BC-B-5 at pH 2

		Langmuir			Freundlich		
Materials	pH	q_m	K_L	R^2	n	K_F	R^2
S-nZVI/BC-C-5	2	398.9	1.1272	0.9721	17.02	297.3	0.9333
S-nZVI/BC-B-5	2	338.9	0.0326	0.9575	3.68	69.60	0.9194

3.6 Cyclic adsorption experiments on Cr(VI) adsorption by S-nZVI/BC-C-5 and S-nZVI/BC-B-5

Cr(VI) adsorption by S-nZVI/BC-C-5 and S-nZVI/BC-B-5 during cyclic experiments is shown in Fig. 7. This figure shows that the adsorption capacities of both materials for Cr(VI) decreased significantly. Setting the initial adsorption capacity as 100%, the adsorption capacity of S-nZVI/BC-B-5 for Cr(VI) dropped by 97.96% in the second cycle, and in subsequent cycles, the adsorption capacity was nearly zero. However, the adsorption capacity of S-nZVI/BC-C-5 for Cr(VI) decreased by 75.79% in the second cycle, with a slower decline in subsequent cycles. After five cycles, the adsorption capacity of S-nZVI/BC-C-5 decreased by 85.96% but reached 42.74 mg g^{-1}. This difference in performance is primarily attributed to the structural features of S-nZVI/BC-C-5. Most of the ZVI in S-nZVI/BC-C-5 is embedded within its spherical structure, allowing the unreacted ZVI to remain available for continued reaction with Cr(VI) during subsequent cycles.

The concentrations of Fe ions in the solution after the first, second, and third cycles of Cr(VI) adsorption on S-nZVI/BC-C-5 were 4.67, 0.26, and 0.12 mg L^{-1}, respectively. In subsequent cycles, no Fe ions were detected in the solution. For S-nZVI/BC-B-5, the concentrations of Fe ions after the first and second cycles of Cr(VI) adsorption were 0.83 and 0.10 mg L^{-1}, respectively, but no iron ions were detected in the solution in later cycles. Fe leaching experiments indicated that the majority of S-nZVI was consumed during the first cycle. In the subsequent adsorption cycles, Cr(VI) was primarily immobilized through adsorption.

3.7 Mechanistic analysis

XRD was used to investigate the crystal structures of S-nZVI/BC-C-5, S-nZVI/BC-C-5–Cr (after two adsorption cycles), S-nZVI/BC-B-5 and S-nZVI/BC-B-5–Cr (after two adsorption cycles). Fig. 8 shows that S-nZVI/BC-C-5 exhibited two intense characteristic diffraction peaks at 2θ = 44.67° and 65.02°, corresponding to the (110) and (200) crystallographic planes of Fe^0, respectively

Table 3 Comparison of adsorption properties of various materials for Cr(VI)

Adsorbents	pH	Concentration range (mg L^{-1})	Q_{max} (mg g^{-1})	Ref.
Chitosan-based adsorbent	1–7	50–500	290.77	42
CAP@Ui0-66-NH_2@PPy hybrid fibrous membrane	2–10	10–50	312.70	43
Iron-rich biochar	2–8	10–800	200	44
Amino-functionalized agricultural waste loofah	2–11	25–400	162.04	45
Fe-based metal organic framework/chitosan composite	3–11	10–200	79.16	46
Graphene aerogel with three-dimensional soft layered structure	1–10	50–250	20.62	47
Fe_3O_4 modified L-glutamic acid functionalized graphene oxide	2–14	15–35	75.63	48
S-nZVI/BC-C-5	2–7	50–300	398.9	This study

(PDF#06-0696).[49] A weak diffraction peak was observed at 2θ = 41.85°, corresponding to the (203) crystal plane of FeS (PDF#65-3356).[50] Another weak peak was observed at 2θ = 60.9°, corresponding to the (112) crystal plane of FeS_2 (PDF#65-2567).[51] The XRD pattern of S-nZVI/BC-B-5 displayed a diffraction peak at 2θ = 44.67°, attributed to the (110) crystal plane of Fe^0 (PDF#06-0696), and another peak at 2θ = 35.5°, assigned to the (201) crystal plane of FeS (PDF#65-3356). For S-nZVI/BC-B-5–Cr, the characteristic diffraction peaks of Fe and FeS largely disappeared. This is primarily because Fe and FeS in S-nZVI/BC-B-5 are mainly loaded on the surface of biochar, where they react rapidly and are extensively consumed during Cr(VI) removal. In the XRD pattern of S-nZVI/BC-C-5–Cr, the diffraction peaks of FeS and FeS_2 were also mostly absent; only relatively weak characteristic Fe diffraction peaks were detected. This indicates that Fe is primarily encapsulated within the spherical nZVI/BC-B-5, allowing a portion of Fe to participate in subsequent adsorption reactions.

In the XPS Cr 2p spectrum of S-nZVI/BC-C-5–Cr and S-nZVI/BC-B-5–Cr (Fig. 9a), the Cr $2p_{3/2}$ and Cr $2p_{1/2}$ absorption peaks were fitted into two peaks. The peaks at 576.4 and 586.2 eV corresponded to Cr^{3+} $2p_{3/2}$ and Cr^{3+} $2p_{1/2}$ respectively, and those at 578.3 and 587.9 eV corresponded to Cr^{6+} $2p_{3/2}$ and Cr^{6+} $2p_{1/2}$, respectively.[40] These peaks mainly resulted from adsorbed Cr(VI) and Cr(III). The intensity of the Cr diffraction peak for the S-nZVI/BC-C-5–Cr surface was higher than that for the S-nZVI/BC-B-5–Cr surface, which is consistent with the stronger adsorption performance of S-nZVI/BC-C-5 for Cr(VI).

The XPS results for S in S-nZVI/BC-C-5 are shown in Fig. 9b. The S 2p absorption peak was fitted into three components. The peak at 162.98 eV, accounting for 46% of the total area, was attributed to S^{2-}.[41–43] The peak at 164.0 eV, accounting for 39% of the area, was assigned to S_2^{2-},[41–43] and the peak at 167.8 eV, contributing 15%, was associated with SO_4^{2-}.[41–43] Furthermore, the S 2p spectrum of S-nZVI/BC-B-5 was fitted into two peaks, with S^{2-} accounting for 23% and SO_4^{2-} for 77% of the total area.[41–43] No S_2^{2-} peak was detected.

Fig. 9c shows the XPS analysis of Fe in S-nZVI/BC-C-5 and S-nZVI/BC-C-5–Cr. For S-nZVI/BC-C-5, the peak at 719.0 eV accounted for 14% of the total peak area and was attributed to Fe^0.[52,53] The peaks at 710.30 and 723.67 eV, accounting for 58%, were assigned to Fe(II),[52,53] while the peaks at 712.70 and 725.80 eV, contributing 28%, were associated with Fe(III).[52,53] After Cr(VI) adsorption, the S-nZVI/BC-C-5–Cr spectrum showed that the Fe(III) content increased to 31%, Fe^0 content decreased to 13%, and Fe(II) content reduced to 56%. This change likely

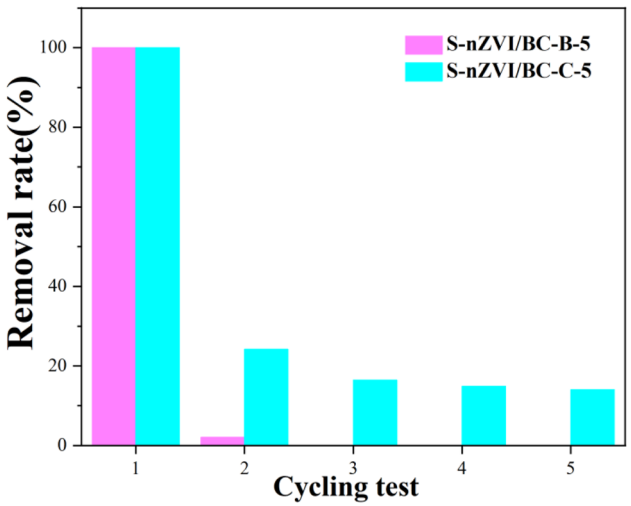

Fig. 7 Cyclic experiments in the adsorption of Cr(VI) by S-nZVI/BC-C-5 and S-nZVI/BC-B-5.

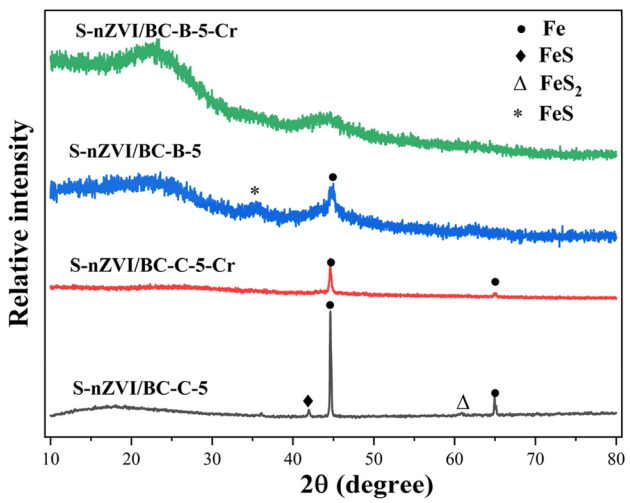

Fig. 8 XRD patterns of S-nZVI/BC-C-5 and S-nZVI/BC-B-5 before and after Cr(VI) adsorption.

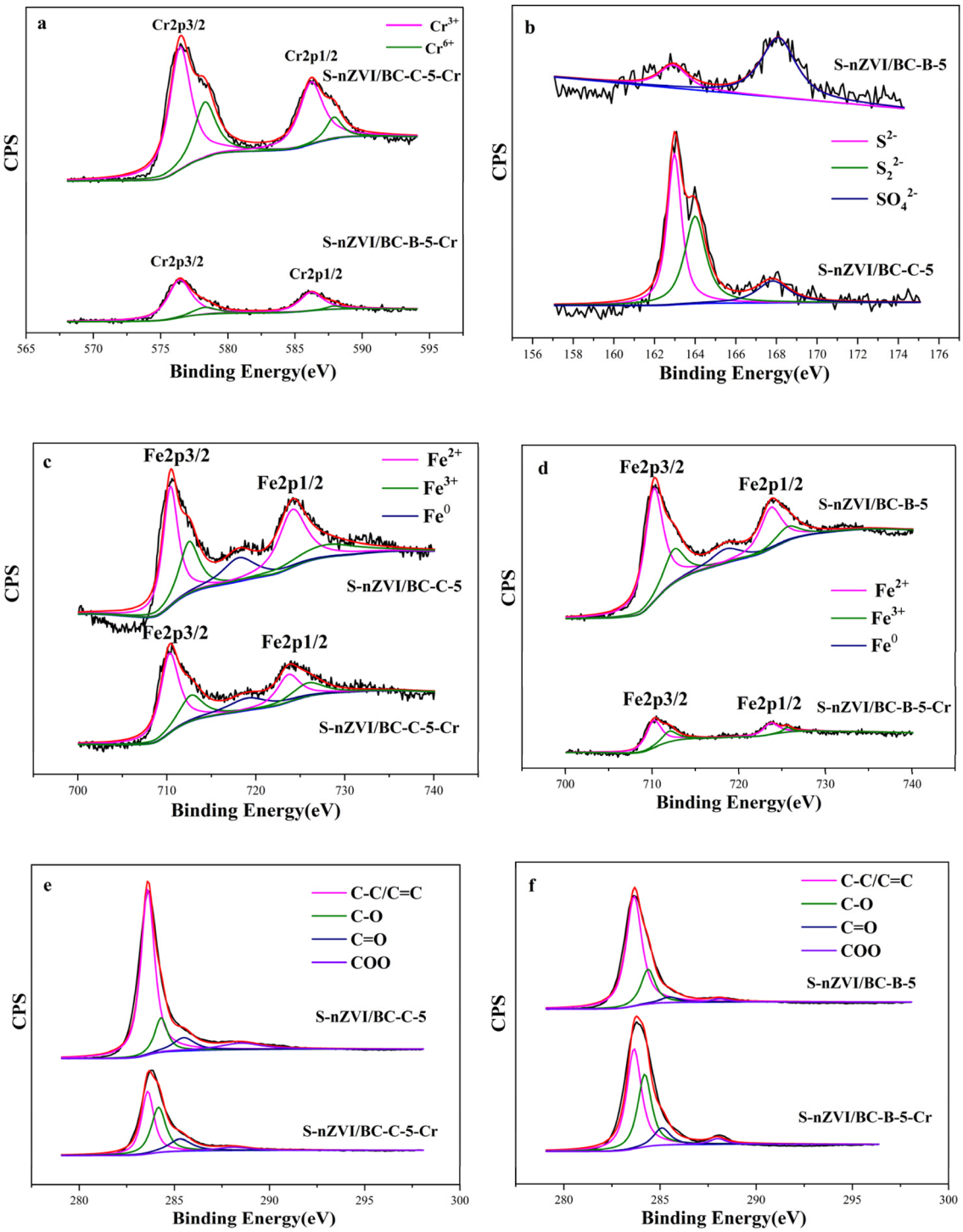

Fig. 9 Cr 2p XPS spectra (a) of S-nZVI/BC-C-5–Cr and S-nZVI/BC-B-5–Cr; S 2p XPS spectra (b) of S-nZVI/BC-C-5 and S-nZVI/BC-B-5; Fe 2p XPS spectra (c) of S-nZVI/BC-C-5 and S-nZVI/BC-C-5–Cr; Fe 2p XPS spectra (d) of S-nZVI/BC-B-5 and S-nZVI/BC-B-5–Cr; C 1s XPS spectra (e) of S-nZVI/BC-C-5 and S-nZVI/BC-C-5–Cr; C 1s XPS spectra (f) of S-nZVI/BC-B-5 and S-nZVI/BC-B-5–Cr.

resulted from a redox reaction in which Fe^0 reduced Cr(VI) to Cr(III), forming Fe(II), which was subsequently oxidised to Fe(III). Fig. 9d presents the Fe 2p spectra of S-nZVI/BC-B-5 and S-nZVI/BC-B-5–Cr. After Cr(VI) adsorption, the characteristic peak of Fe^0 disappeared, which aligns with the cyclic adsorption test results shown in Fig. 7.

The XPS analysis results for C in S-nZVI/BC-C-5 and S-nZVI/BC-C-5–Cr are shown in Fig. 9e. The fitted peaks included C–C/C=C (283.6 eV),[53,54] C–O (284.3 eV),[53,54] C=O (285.5 eV)[53,54] and COO (288.5 eV).[53,54] For S-nZVI/BC-C-5–Cr, the C–C/C=C peak position remained unchanged, while the C–O, C=O and COO peaks were weaker than those of S-nZVI/BC-C-5, suggesting that

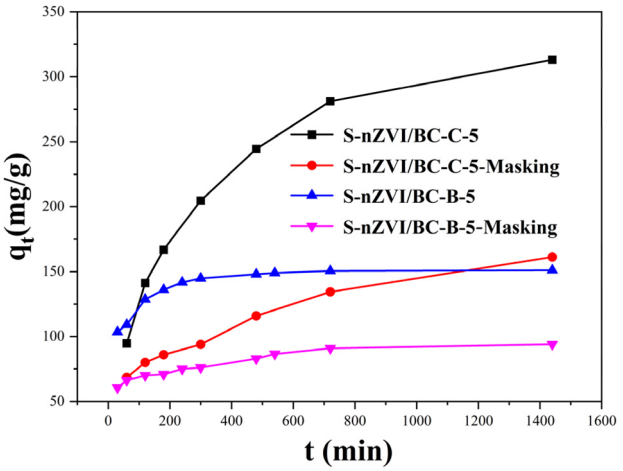

Fig. 10 Masking experiments of S-nZVI/BC-C-5 and S-nZVI/BC-B-5 for Cr(VI) adsorption.

C–O, C=O and COO participated in Cr(VI) or Cr(III) adsorption, likely forming complexes and reducing binding energy.[55] Fig. 9f displays the C 1s spectra of S-nZVI/BC-B-5 and S-nZVI/BC-B-5–Cr. The trends in the binding energies of the C–C/C=C, C–O, C=O and COO peaks were consistent with those observed in the binding energies of these peaks for S-nZVI/BC-C-5 and S-nZVI/BC-C-5–Cr.

According to Fig. 10, the addition of 1 g per L 1,10-phenanthroline considerably inhibited the adsorption of Cr(VI) by both S-nZVI/BC-C-5 and S-nZVI/BC-B-5. This is primarily attributed to the formation of a stable orange–red complex between 1,10-phenanthroline and Fe^{2+}, which reduces the concentration of free Fe^{2+} in the solution, thereby diminishing Cr(VI) adsorption. These findings confirm that the reduction of Cr(VI) by Fe^{2+} is the dominant mechanism governing its removal.

Based on the results of XRD, XPS and the masking experiment, a reaction mechanism for Cr(VI) adsorption by S-nZVI/BC-C-5 is proposed. Initially, Cr(VI) is reduced to Cr(III) by nZVI, during which nZVI is oxidised to Fe(II) (eqn (7) and (8)).[33,56] The oxidation of nZVI generates a substantial amount of Fe(II), while the FeS shell corrodes to produce HS^- (eqn (9)).[18,57,58] Subsequently, Cr(VI) is reduced by the released Fe^{2+} and HS^- (ref. 57 and 58) (eqn (10)–(13)). In addition, Cr(VI) accepts electrons from FeS and FeS_2 in the shell, accompanied by the oxidation of S^{2-} and S_2^{2-} to SO_4^{2-} (eqn (14) and (15)).[10] The overall adsorption process is schematically illustrated in Fig. 11. The major mechanisms involved in Cr(VI) removal are as follows: (i) reduction of Cr(VI) to Cr(III) by Fe, FeS and FeS_2; (ii) reduction of Cr(VI) by Fe^{2+}; (iii) reduction of Cr(VI) by HS^- generated from FeS corrosion; and (iv) physical adsorption of Cr species by biochar and metal oxides. S-nZVI/BC-B-5 exhibits a similar Cr(VI) removal mechanism as S-nZVI/BC-C-5.

$$3Fe + Cr_2O_7^{2-} + 14H^+ \rightarrow 3Fe^{2+} + 2Cr^{3+} + 7H_2O \quad (7)$$

$$3Fe + 2HCrO_4^- + 14H^+ \rightarrow 3Fe^{2+} + 2Cr^{3+} + 8H_2O \quad (8)$$

$$FeS + H^+ \rightarrow Fe^{2+} + HS^- \quad (9)$$

$$3HS^- + 4Cr_2O_7^{2-} + 29H^+ \rightarrow 8Cr^{3+} + 16H_2O + 3SO_4^{2-} \quad (10)$$

$$3HS^- + 8HCrO_4^- + 29H^+ \rightarrow 8Cr^{3+} + 20H_2O + 3SO_4^{2-} \quad (11)$$

$$Fe^{2+} + Cr_2O_7^{2-} + 14H^+ \rightarrow 6Fe^{3+} + 2Cr^{3+} + 7H_2O \quad (12)$$

$$3Fe^{2+} + HCrO_4^- + 7H^+ \rightarrow 3Fe^{3+} + Cr^{3+} + 4H_2O \quad (13)$$

$$2FeS + 3Cr_2O_7^{2-} + 26H^+ \rightarrow 2Fe^{3+} + 6Cr^{3+} + 13H_2O + 2SO_4^{2-} \quad (14)$$

$$3FeS_2 + 15HCrO_4^- + 57H^+ \rightarrow 3Fe^{3+} + 15Cr^{3+} + 36H_2O + 6SO_4^{2-} \quad (15)$$

3.8 Remediation of simulated Cr(VI) wastewater using S-nZVI/BC-C-5 and S-nZVI/BC-B-5

The Cr(VI) adsorption capacity for S-nZVI/BC-C-5 and S-nZVI/BC-B-5 in the blank control group was set as 100%. As shown in Fig. 12, the Cr(VI) removal efficiency for both materials increased in the presence of background electrolytes, including

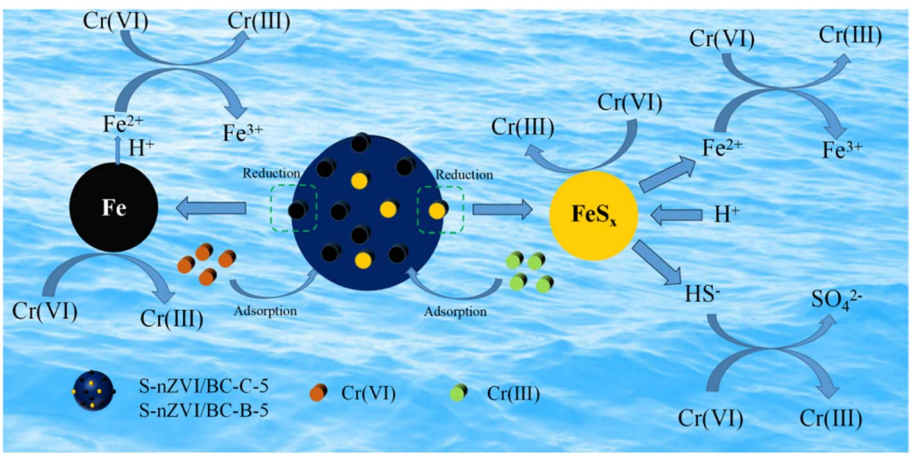

Fig. 11 Schematic of the mechanism of Cr(VI) adsorption on S-nZVI/BC-C-5 and S-nZVI/BC-B-5.

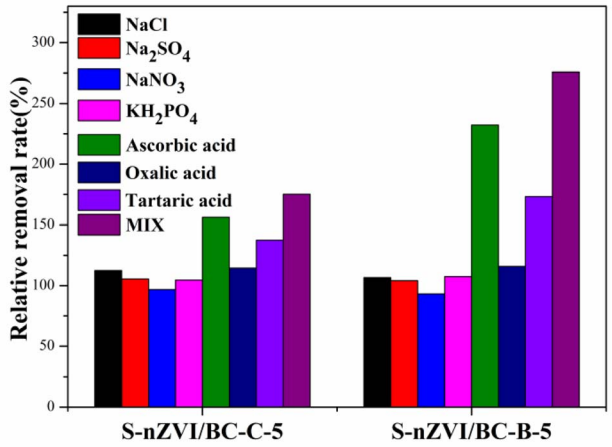

Fig. 12 Remediation of simulated Cr(VI) wastewater by S-nZVI/BC-C-5 and S-nZVI/BC-B-5.

NaCl, Na_2SO_4, KH_2PO_4, tartaric acid, ascorbic acid, oxalic acid and a mixed-ion solution. Chloride ions (Cl^-), as Lewis bases, exhibited a corrosive effect on the passivation layer of iron oxides. They could easily penetrate the oxide film on the surface of S-nZVI, causing varying degrees of pitting corrosion. This localised corrosion created new reactive sites, thereby overcoming passivation-induced barriers and enhancing Cr(VI) adsorption.[59] The iron oxides on the S-nZVI surface demonstrated a strong affinity for sulphate ions (SO_4^{2-}).[11] These ions displaced surface hydroxyl groups (–OH) and formed monodentate or bidentate complexes with surface iron atoms. The formation of such complexes accelerated the corrosion of S-nZVI, leading to the release of more sulphide ions (S^{2-}), which actively participated in the reduction of Cr(VI).[60] Phosphate ions ($H_2PO_4^-$) likely enhanced Cr(VI) reduction by forming ternary surface complexes (*e.g.* $\equiv H_2PO_4^- - CrO_4^{2-}$) on the S-nZVI surface. These complexes promoted electron transfer and increased material reactivity. Furthermore, phosphate could react with reduced Cr(III) to form insoluble $CrPO_4$, effectively reducing the concentration of dissolved Cr(III).[61] This removal shifted the reaction equilibrium toward Cr(VI) reduction, thereby improving the overall removal efficiency. It was obvious that NO_3^- influenced the Cr(VI) removal to some extent because NO_3^- can be reduced to NO_2^- or NH_4^+ by nZVI, competing with Cr(VI).[18] Ascorbic acid can substantially enhance the Cr(VI) removal performance of S-nZVI/BC-C-5 and S-nZVI/BC-B-5, primarily due to its strong reducing properties; it rapidly reduces Cr(VI) to Cr(III) while being oxidised to dehydroascorbic acid.[62] Tartaric acid also markedly improves the Cr(VI) reduction rate by reducing Cr(VI) to Cr(III).[63] In addition, oxalic acid increases the Cr(VI) reduction rate.[64] Since most background ions promote the Cr(VI) removal by S-nZVI/BC-C-5 and S-nZVI/BC-B-5, the experimental group with mixed background ions exhibits the highest Cr(VI) removal rate.

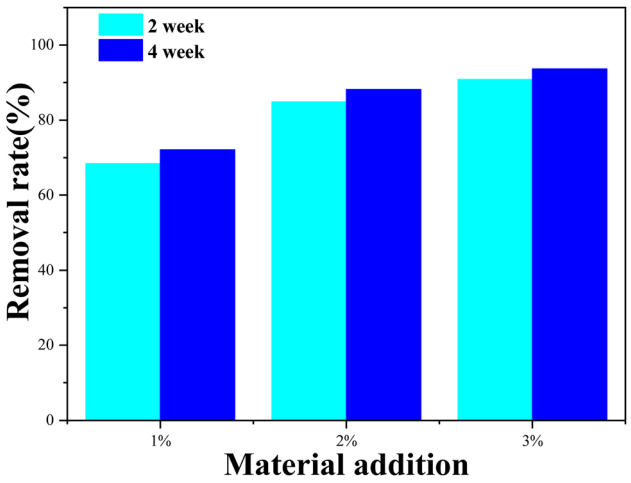

Fig. 13 Experimental results on the remediation of Cr(VI)-contaminated soil by S-nZVI/BC-C-5.

3.9 Remediation of Cr(VI) pollution in soil by S-nZVI/BC-C-5

The experimental outcomes of the remediation of simulated soil contaminated with Cr(VI) using S-nZVI/BC-C-5 are shown in Fig. 13. The Cr(VI) content decreased by 68.4%, 84.9% and 90.8% after 14 d of remediation of the soil sample when using 1%, 2% and 3% w/w mixtures, respectively, of S-nZVI/BC-C-5 and soil. After 28 d of treatment, the Cr(VI) content decreased by 72.1%, 88.2% and 92.6%, respectively. When the dosage of S-nZVI/BC-C-5 increased from 1% to 3% (w/w), the removal of Cr(VI) from contaminated soil gradually increased. Upon the addition of 3% S-nZVI/BC-C-5 (w/w), the removal rate of Cr(VI) was similar for days 14 and 28.

4. Conclusions

Herein, S-nZVI/BC-C-5 was prepared *via* the sulphidation of BC@Fe, while S-nZVI/BC-B-5 was synthesised using a one-step $NaBH_4$ reduction method with Fe^{3+} as the iron source and Na_2S as the sulphur source. S-nZVI/BC-C-5 exhibited markedly superior Cr(VI) adsorption performance compared with S-nZVI/BC-B-5. The kinetic data for Cr(VI) adsorption by S-nZVI/BC-C-5 and S-nZVI/BC-B-5 at pH 2 were consistent with the pseudo-second-order models, which yielded the equilibrium adsorption capacities of 309.8 and 143.7 mg g^{-1}, respectively. XRD, XPS, and Fe^{2+} masking results demonstrate that the dominant adsorption mechanisms of S-nZVI/BC-C-5 are direct reduction and corrosive reduction of Cr(VI), mainly involving (i) reduction of Cr(VI) to Cr(III) by FeS, FeS_2 and Fe^0; (ii) reduction by Fe^{2+}; (iii) reduction by HS^- generated through FeS corrosion; and (iv) adsorption of Cr(VI) by biochar and surface metal oxides. In terms of reusability, S-nZVI/BC-C-5 demonstrated greater stability, retaining an adsorption capacity of 42.74 mg g^{-1} after five cycles, whereas S-nZVI/BC-B-5 lost all adsorption effectiveness after the second cycle. Wastewater remediation tests confirmed that the presence of co-existing ions slightly enhanced Cr(VI) removal by S-nZVI/BC-C-5, reflecting strong anti-interference capability. Moreover, soil remediation experiments revealed that the addition of 3% S-nZVI/BC-C-5 to Cr(VI)-contaminated soil achieved a 92.6% reduction in Cr(VI) content

after 28 d. These results demonstrate that S-nZVI/BC-C-5 is a cost-effective and highly efficient material with substantial potential for practical application in the remediation of Cr(VI)-polluted water and soil environments.

Conflicts of interest

The authors declare that they have no known competing financial interests or personal relationships that could have appeared to influence the work reported in this paper.

Data availability

All relevant data are within the manuscript and its additional files.

Acknowledgements

This work was supported by Hainan S&T Program (Project No. ZDYF2024GXJS301; ZDYF2022SHFZ279). Haikou Science and Technology Special Fund (Project No. 2024-011).

References

1 P. Han, J. Xie, X. Qin, X. Yang and Y. Zhao, *Sci. Total Environ.*, 2022, **828**, 154422.
2 J. Xu, R. Bao, C. Wei, J. Xia, T. Wang, W. Liu and X. Xing, *J. Environ. Chem. Eng.*, 2022, **10**, 108412.
3 S. Prasad, K. K. Yadav, S. Kumar, N. Gupta, M. M. S. Cabral-Pinto, S. Rezania, N. Radwan and J. Alam, *J. Environ. Manage.*, 2021, **285**, 112174.
4 Z. Yang, X. Zhang, Z. Jiang, Q. Li, P. Huang, C. Zheng, Q. Liao and W. Yang, *Sci. Total Environ.*, 2021, **773**, 145654.
5 X.-Y. Huang, W. Wang, L. Ling and W.-X. Zhang, *Acta Chim. Sin.*, 2017, **75**, 529.
6 Z. Yuan, A. Peng, Z. Chu, X. Zhang, H. Huang, Y. Mi, D. Xia, X. Wu, Z. Ye, Y. Tao and X. Yan, *Sci. Total Environ.*, 2024, **921**, 171107.
7 Y. Wang, H. Li, W. Xia, L. Yu, Y. Yao, X. Zhang and H. Jiang, *J. Mol. Liq.*, 2023, **390**, 123089.
8 X. Zhang, Q. Li, K. Nie, K. Cao, Q. Liao, M. Si, Z. Yang and W. Yang, *Chemosphere*, 2023, **321**, 138132.
9 W. Jiao, Y. Song, D. Zhang, G. Chang, H. Fan and Y. Liu, *Adv. Powder Technol.*, 2019, **30**, 2251–2261.
10 K. Li, W. Xu, H. Song, F. Bi, Y. Li, Z. Jiang, Y. Tao, J. Qu and Y. Zhang, *Sci. Total Environ.*, 2024, **907**, 168133.
11 M. Bhattacharya, N. H. Barbhuiya and S. P. Singh, *Groundw. Sustain. Dev.*, 2024, **26**, 101196.
12 Z. Hu, J. Rao, Z. Xie, M. Liu, L. Su, Y. Chen, W. Gao, Y. Tan, Z. Zhou and N. Zhou, *J. Water Proc. Eng.*, 2023, **51**, 103424.
13 K. Yang, X. Wang, I. Lynch, Z. Guo, P. Zhang, L. Wu and J. Ma, *J. Hazard. Mater.*, 2023, **442**, 129923.
14 J. Zhan, M. Ma, X. Zhang, M. Li, Y. Zhang, H. Zhou and T. Wang, *J. Environ. Chem. Eng.*, 2023, **11**, 110242.
15 W. Mao, Y. Li, L. Zhang, X. Shen, Y. Liu and Y. Guan, *Chem. Eng. J.*, 2024, **487**, 150518.
16 S. K. Mohamed, A. O. Abd El-Aziz, A. M. Elazhary and A. B. Azzam, *Appl. Water Sci.*, 2025, **15**, 85.
17 X. Zhang, H. Xu, M. Xi and Z. Jiang, *J. Environ. Chem. Eng.*, 2023, **11**, 109860.
18 H. Tian, C. Huang, P. Wang, J. Wei, X. Li, R. Zhang, D. Ling, C. Feng, H. Liu, M. Wang and Z. Liu, *Bioresour. Technol.*, 2023, **369**, 128452.
19 J. Guo, F. Gao, C. Zhang, S. Ahmad and J. Tang, *Chem. Eng. J.*, 2023, **477**, 147049.
20 J. Zhang, L. Xie, Q. Ma, Y. Liu, J. Li, Z. Li, S. Li and T. Zhang, *Chemosphere*, 2022, **311**, 137174.
21 A. Wang, J. Hou, C. Tao, L. Miao, J. Wu and B. Xing, *Environ. Sci. Technol.*, 2023, **57**, 3323–3333.
22 M. Yuan, J. Xin, X. Wang, F. Zhao, L. Wang and M. Liu, *Water Res.*, 2022, **216**, 118286.
23 L. Qian, Y. Long, H. Li, Z. Wei, C. Liang, R. Liu and M. Chen, *Sci. Total Environ.*, 2023, **889**, 164243.
24 W. Du, Y. Zhang, Y. Li, X. Ma and C. Zhao, *J. Nanopart. Res.*, 2023, **25**, 119.
25 C. Zhou, C. Han and N. Liu, *J. Environ. Sci.*, 2024, **135**, 232–241.
26 Z. Ye, Y. Liu, J. Xu, N. Xu, J. Dong, H. Chen, D. Li, L. Peng, Y. Gao and J. Zhao, *ACS ES&T Water*, 2024, **4**, 1853–1863.
27 X. Zhang, Y. He, Q. Li, Q. Liao, M. Si, Z. Yang and W. Yang, *J. Soils Sediments*, 2024, **24**, 1988–2000.
28 J. Tan, K. Hong, G. Shen and Y. Yan, *Catal. Commun.*, 2022, **172**, 106553.
29 L. Shao, J. Hong, S. Wang, F. Wu, F. Yang, X. Shi and Z. Sun, *J. Power Sources*, 2021, **491**, 229627.
30 W. Huang, Y. Tang, X. Zhang, Z. Luo and J. Zhang, *J. Water Proc. Eng.*, 2022, **45**, 102470.
31 C. Yu, D. Zhang, X. Dong and Q. Lin, *RSC Adv.*, 2018, **8**, 34151–34160.
32 X. Zhou, G. Jing, B. Lv, Z. Zhou and R. Zhu, *Chemosphere*, 2016, **160**, 332–341.
33 X. Xing, X. Ren, N. S. Alharbi and C. Chen, *J. Colloid Interface Sci.*, 2023, **629**, 744–754.
34 A. B. Azzam, A. O. Abd El-Aziz and S. K. Mohamed, *Sep. Purif. Technol.*, 2022, **284**, 120238.
35 C. Zhou, C. Han and N. Liu, *J. Environ. Sci.*, 2024, **135**, 232–241.
36 D. Hou, X. Cui, M. Liu, H. Qie, Y. Tang, W. Leng, N. Luo, H. Luo, A. Lin, W. Yang, W. Wei and T. Zheng, *Sci. Total Environ.*, 2024, **908**, 168341.
37 T. Zheng, D. Hou, N. Wu, M. Wang, N. Luo, H. Luo, W. Leng, P. Li and W. Wei, *J. Environ. Chem. Eng.*, 2023, **11**, 111573.
38 T. Wang, Y. Sun, L. Bai, C. Han and X. Sun, *Sep. Purif. Technol.*, 2023, **306**, 122631.
39 J. Ma, N. Jia, H. Jin, S. Yao, K. Zhang, Y. Kai, W. Wu and Y. Wen, *Sep. Purif. Technol.*, 2023, **317**, 123880.
40 Y. Yi, X. Wang, Y. Zhang, K. Yang, J. Ma and P. Ning, *Adv. Powder Technol.*, 2023, **34**, 103826.
41 M. E. González-López, C. M. Laureano-Anzaldo, A. A. Pérez-Fonseca, M. Arellano and J. R. Robledo-Ortíz, *Sep. Purif. Rev.*, 2020, **50**, 333–362.
42 L. Peng, Z. Hu, J. Cui, N. Yang, R. Bao, Y. Dai, Q. Wang, Y. Jiang and P. Cui, *Sep. Purif. Technol.*, 2025, **360**, 131055.

43 T. Li, Z. Huang, M. Hu, Y. Hu, K. Quan, M. Zhou, Y. Chen and S. Fu, *Chem. Eng. J.*, 2025, **509**, 161213.
44 Y. Zeng, L. Zhou, X. Wang, G. Zhang, X. Bao, Z. Yan and W. Ma, *J. Environ. Chem. Eng.*, 2025, **13**, 115701.
45 Y. Zhao, T. Chen, T. Liang, Y.-Y. Tian, L.-F. Chen, B. Li and J. Gao, *Colloids Surf., A*, 2025, **715**, 136693.
46 K. Li, Z. Yang, D. Sun, Z. Chen, D. Chen and P. Lu, *Sep. Purif. Technol.*, 2025, **369**, 133115.
47 Y. Zheng, H. Li, L. You, Q. Yang, D. Lei, D. Chen and W. Zhan, *J. Environ. Chem. Eng.*, 2025, **13**, 116727.
48 M. Liu, Y. Wang, Y. Chen, T. Zhang, Z. Zhang, H. Li, F. Shan and T. Ma, *Sep. Purif. Technol.*, 2025, **363**, 132090.
49 Y. Zhang, B. Chen, Y. Qiao, Y. Duan, X. Qi, S. He, H. Zhou, J. Chen, A. Yuan and S. Zheng, *J. Mater. Sci. Technol.*, 2024, **201**, 157–165.
50 H. Zhang, Y. Meng, W. Hafiz Zaki Ahmed, J. Hu, M. Xiao, F. Zhu and Y. Zhang, *J. Electroanal. Chem.*, 2021, **886**, 115102.
51 H. Jia, J. Li, L. Wang, Z. Huang and J. Xu, *Int. J. Electrochem. Sci.*, 2020, **15**, 10653–10663.
52 T. Jiang, B. Wang, B. Gao, N. Cheng, Q. Feng, M. Chen and S. Wang, *J. Hazard. Mater.*, 2023, **442**, 130075.
53 J. Zhao, Y. Qin, Y. Liu, Y. Shi, Q. Lin, M. Cai, Z. Jia, C. Yu, A. Shang, Y. Fei and J. Zhang, *Molecules*, 2024, **29**, 1595.
54 W. Xue, J. Li, X. Chen, H. Liu, S. Wen, X. Shi, J. Guo, Y. Gao, J. Xu and Y. Xu, *Environ. Sci. Pollut. Res. Int.*, 2023, **30**, 101933–101962.
55 Y. Shi, R. Shan, L. Lu, H. Yuan, H. Jiang, Y. Zhang and Y. Chen, *J. Clean. Prod.*, 2020, **254**, 119935.
56 S. Wang, D. Zhong, Y. Xu and N. Zhong, *New J. Chem.*, 2021, **45**, 13969–13978.
57 Y. Xi, Y. Wu, Y. Liu, T. Xie, H. Liu, Z. Su, Y. Huang, X. Yuan, C. Zhang and X. Li, *Chem. Eng. J.*, 2022, **448**, 137610.
58 Z. Lin, C. Zheng, J. Ren, A. Zhu, C. He and H. Pan, *Colloids Surf., A*, 2023, **667**, 131376.
59 Y. F. Su, C. Y. Hsu and Y. H. Shih, *Chemosphere*, 2012, **88**, 1346–1352.
60 M. C. Mangayayam, V. Alonso-de-Linaje, K. Dideriksen and D. J. Tobler, *Chemosphere*, 2020, **249**, 126137.
61 R. Zhang, H. Sun and J. Yin, *Front. Environ. Sci. Eng. China*, 2008, **2**, 203–208.
62 Q. Zaib, H. S. Park and D. Kyung, *Sci. Rep.*, 2021, **11**, 13136.
63 A. B. Azzam, N. A. Edress, F. M. El-Dars and A. O. Abd El-Aziz, *Int. J. Environ. Anal. Chem.*, 2024, 1–19.
64 A. Nurjanah, B. Rumhayati and A. Wiryawan, *IOP Conf. Ser.:Mater. Sci. Eng.*, 2020, **833**, 012029.